Generation of bimodal solitons in a sapphire whispering-gallery-mode maser at millikelvin temperatures

Catriona A. Thomson, Michael E. Tobar, and Maxim Goryachev[*]

ARC Centre of Excellence for Engineered Quantum Systems and ARC Centre of Excellence for Dark Matter Particle Physics, Department of Physics, University of Western Australia, 35 Stirling Highway, Crawley WA 6009, Australia

We present experimental observations of bimodal solitons in a solid state three-level maser cooled to millikelvin temperatures. The maser is built on a highly dilute Fe^{3+} spin ensemble hosted by a high-purity Al_2O_3 crystal constituting a high-quality factor whispering-gallery-mode resonator. The maser is pumped through one of these modes, near 31 GHz, generating two signals near 12.04 GHz from two distinct modes, 8 MHz apart. The system demonstrates three regimes, namely, a continuous-wave regime, a dense soliton regime, and a sparse soliton regime. These results open other avenues for studying nonlinear wave phenomena using microwave systems as well as different applications of solitons in this part of the electromagnetic spectrum.

I. INTRODUCTION

Optical frequency combs have become key in myriad applications from metrology and precision spectroscopy to tests of beyond the standard model physics, with their remarkable ability to compare clocks within 10^{-19} Hz [1,2]. Initially produced via mode-locked lasers [3–5], which revolutionized the field of frequency metrology [6,7], a particularly active area of current research is in developing alternative production mechanisms for such combs, in engineering systems balanced between nonlinear gain and dissipation.

A frequency comb may occur in conjunction with solitons within a resonator, equivalent to ultrashort phase-locked pulses circulating the cavity in the time domain. Such pulses may be infinitely supported within the resonator, given a continuous-wave pump source and a resonant medium which displays a balance between dispersion and nonlinear gain [8]. To this end, the nonlinear Kerr effect has been much exploited as the dissipative structure in various material systems [8–10] such as silica optical fibers [11], and high-Q crystalline and silicon nitride-based microresonators [8,12].

Despite such a plethora of systems demonstrating combs and solitons [13], they are quite unique to the optical frequency domain. This article reports an observation of microwave solitons in a maser system. The reported phenomena were produced via the iron paramagnetic impurities (order of parts per billion) within the most pure HEMEX-grade synthetic sapphire crystal, when cooled to millikelvin temperatures and with zero applied magnetic field [14]. The paramagnetic impurities have been shown to offer nonlinear gain in form of a χ^3 nonlinearity at 4 K in temperature, which, besides masing [14], has produced four-wave mixing [15], frequency conversion [16], and time-reversal symmetry breaking [17,18]. Dispersion arises from the frequency dependence of the effective permeability and thus refractive index due to these paramagnetic impurities [18] which can be altered by pumping a mode near the ion pump transition. Furthermore, at millikelvin temperature, the effects of paramagnetic impurities on the properties of cooled sapphire resonators have been shown to be enhanced when compared with the effects at 4 K as the majority of the spins condense to the ground state [18–20]. This work reports the operation of such a maser at millikelvin temperatures, with the observation of effects not seen in the 4 K system, providing an avenue for implementing optical metrological methods in the microwave and radio-frequency domains.

II. EXPERIMENTAL SETUP

The experimental setup is based on a cylindrical HEMEX-grade sapphire (undoped monocrystalline α-Al_2O_3) resonator supporting extremely high-quality factor whispering gallery modes (WGMs) in the microwave frequency range. The crystalline lattice of sapphire is host to a number of naturally occurring impurities including Fe^{3+}, Cr^{3+}, and Ti^{3+} with typical concentrations of parts per billion in HEMEX-grade crystals [20]. Our crystal has been annealed to increase the Fe^{3+} population by conversion of Fe^{2+} to Fe^{3+}, with a 100-fold improvement achieved in the Fe^{3+} to Fe^{2+} ratio [21]. Paramagnetic Fe^{3+} ions in sapphire, each substituting an Al^{3+} cation, was proposed [22] and implemented as a gain medium for cryogenic masers, which do not require any external magnetic field [21,23]. Profitably, at zero applied field, this ion represents a three-level system with the spin-$|1/2\rangle$ (ground state), $|3/2\rangle$ (intermediate state), and $|5/2\rangle$ (higher excited) states. These three levels are ideally suited to be used as a Λ scheme: pumping the $|1/2\rangle \rightarrow |5/2\rangle$ transition via a high-frequency pump WGM within the ion's electron spin resonance (ESR) linewidth, inducing a fast nonradiative transition to the intermediate level with a short lifetime, followed by a radiative maser transition $|3/2\rangle \rightarrow |1/2\rangle$, and stimulating
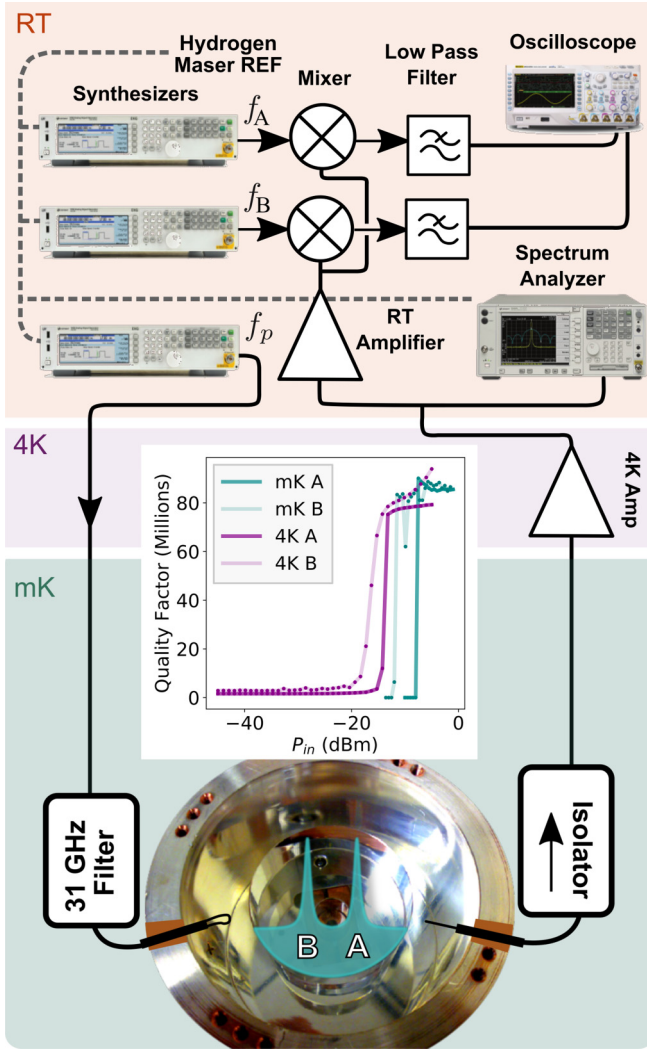
*maxim.goryachev@uwa.edu.au

FIG. 1. Experimental setup used to generate maser solitons at mK temperatures. A WGM crystal resonator is pumped from a room-temperature signal source (around 31 GHz) through an input filter ensuring minimal excitation of the readout mode. Generated maser signals (around 12 GHz) are collected with a single antenna and fed through a low-temperature isolator and a low-noise cryogenic amplifier. These signals are analyzed via a spectrum analyzer and down-converted via two mixers to be observed via an oscilloscope. Inset: Fitted quality factors of modes A and B at 4 K and mK, at a range of powers incident on the modes, without any applied pump mode. These whispering gallery modes require a certain threshold of incident power to be applied to the mode for high-quality factor resonance to be possible.

photon emission at the ESR frequencies around ~12.04 GHz, which happens to encompass the linewidth of two signal WGMs in the crystal (see Fig. 1). These signal WGMs have sufficient quality factors to self-sustain resonance for sufficient pump power. Figure 1 (inset) shows the quality factors of modes A and B, displaying a very strong nonlinearity in the form of quality factor dependence on power incident on the mode.

The sapphire WGM crystal was housed in a silver-plated copper cavity and interrogated by two microwave probes

TABLE I. Target whispering gallery modes.

Pump mode	Frequency (GHz)	Readout mode	Frequency (GHz)
1	31.33771	A	12.03812
2	31.33974	B	12.02979

inserted through the cavity walls. The output probe is an antenna oriented to couple to two modes in the region of 12.04 GHz (specifically, we investigate the responses of mode A at 12.038 12 GHz and mode B at 12.029 79 GHz). The input probe is an orthogonally oriented loop which, ideally, strongly couples to the azimuthal magnetic component of one of the (dominantly transverse-magnetic) modes in the vicinity of the 31.9-GHz transition and does not load quality factors of the signal modes, which are quasi-transverse-electric modes. See Table I for an overview of microwave modes used.

The cavity is attached to the millikelvin stage of a dilution refrigerator. The pump signal is generated by a microwave synthesizer locked to a hydrogen maser and delivered to the cavity via a series of copper and phosphor-bronze cables. The signal is cleaned by a narrow bandpass filter tuned to near 31.5 GHz and directly bolted to the cavity. The total attenuation of the cables and the filter from the output of the synthesizer to the input of the cavity is 31 dB at the pump frequency. The output signals from the crystal pass through a millikelvin isolator and a 4-K low-noise amplifier. At room temperature the target signal is split between a spectrum analyzer, used to collect frequency data around the target mode, and two down-conversion channels, used to mix down the signal for collection of time-series data. To achieve down-conversion, two synthesizers generate frequencies of f_A and f_B to bring the signal carriers to the kHz level whereby they are individually digitized with a two-channel high-speed real-time oscilloscope. A schematic of the experimental setup used to observe maser solitons is shown in Fig. 1.

III. OBSERVATIONS

Masing was observed on two signal modes ($f_A = 12.038\,13$ GHz and $f_B = 12.029\,79$ GHz) for a range of pump frequencies Δf_p, swept around the pump mode, $f_p = 31.337\,71$ GHz. Full spectra of the masing signal from f_A are given in Fig 2, along with snapshots from both f_A and f_B.

A. Comb structure

At millikelvin temperatures (within a dilution fridge cooled to ~16 mK, but transiently heated to ~20–50 mK), a comb-like structure was obtained (Figs. 2 and 3, inset). Comb lines only persist down to approximately −40 dBm incident pump power, below which the comb collapses. Data at 4 K were also obtained, but results are deferred to the Appendixes. It has to be noted that the 4 K and mK regimes for the maser system are sufficiently different. The occupation number of the excited state for the system at 4 K is $n = \frac{1}{e^{\frac{h\nu}{k_B T}} + 1} \approx 0.41$ whereas for 50 mK it is 8.643×10^{-14}.

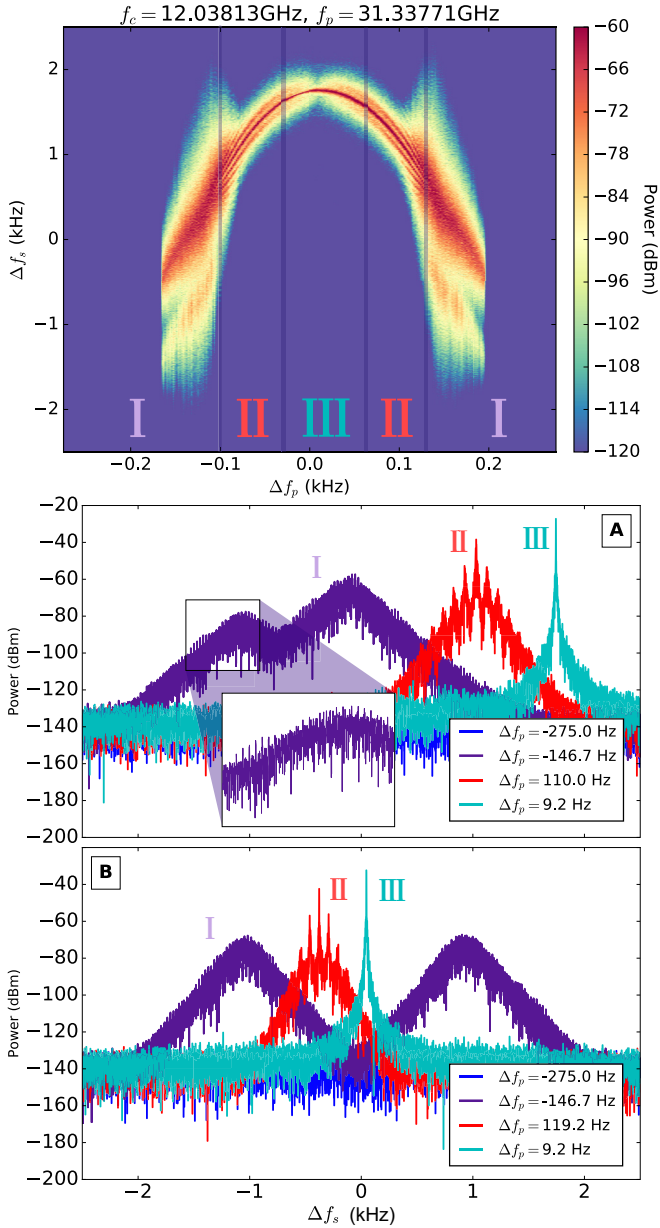Figures 2 and 3 demonstrate three distinct generation regimes: (III) the continuous-wave regime at the center (near

FIG. 2. Top: Spectra of masing on mode A (f_s) for different pump frequencies around 31.3377 GHz (Δf_p). A/B: Snapshots of masing on mode A/B at various Δf_p, illustrating the three masing regimes. Note that f_s is arbitrarily chosen, serving only to indicate scale, as the signal frequency has no unambiguously natural center.

FIG. 3. Top: Spectra of masing on mode A (f_s) for different pump powers at 31.3377 GHz. A/B: Snapshots of masing on mode A/B at various pump powers, illustrating the three masing regimes. Note that f_s is arbitrarily chosen, serving only to indicate scale, as the signal frequency has no unambiguously natural center.

zero Δf_p) with a narrow masing peak, (II) the few peak regime for larger detuning, corresponding to high-density soliton emission, followed by (I), a sparse soliton regime just surpassing the masing threshold on both sides of the masing regime, with few solitons. The latter regime demonstrates a second broad feature that can be attributed to the doublet phenomenon in WGM systems where the solution has two degenerate components. Various symmetry-breaking features in the sapphire resonator lift this degeneracy and our readout mode thus exists as a double-peaked structure. It is worth noting that for the continuous-wave regime with $\Delta f_p \sim 0$, one peak supercedes the other within the doublet.
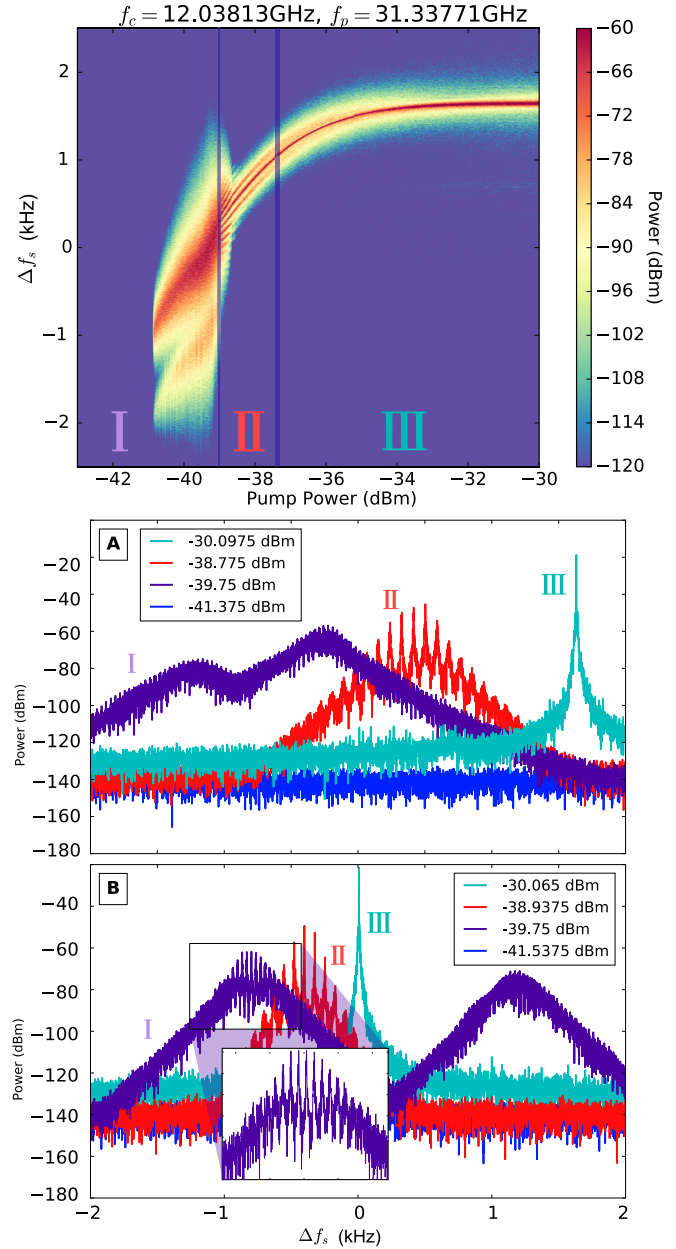
The dependence of the masing regime upon explicitly pump power, at a fixed pump frequency, was also clearly observed (see Fig. 3), displaying analogous regimes to the detuned frequency experiment. Due to the line shape of the WGM pump mode, pumping off resonance delivers less power to the pump transition; hence, either parameter, pump power or pump frequency, can be used to control power delivered to the pump transition. It should be noted that the "bimodality" of the system refers, in fact, to the simultaneous masing on modes A and B, which are separated by $\sim$8 MHz, and not to the doublet phenomenon caused by lifted degeneracy.
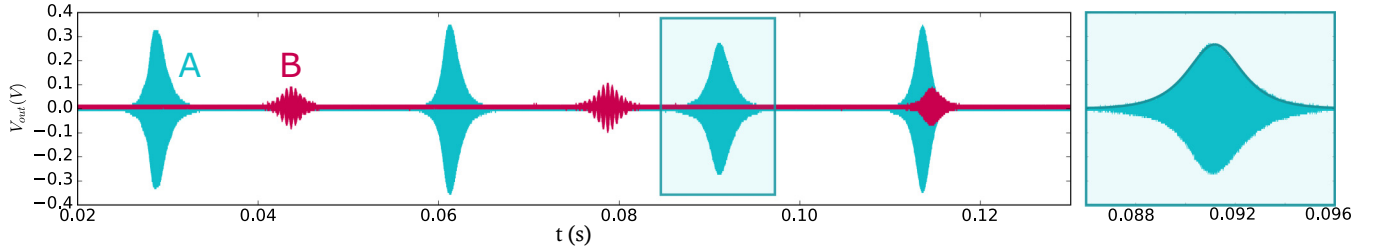
FIG. 4. Time-series output of mode A (blue) and B (pink) of the crystal, in regime I, being pumped at 31.337 707 136 GHz, after being mixed down to baseband, representing modulation of the carrier mode. The soliton pulse train is the time-series equivalent of the comb structure. The fitted *sech* envelope of one pulse is highlighted.

B. Pulse train

Examining the time-series data, this masing can be observed to be expelled in discrete millisecond-scale solitons, the time-domain phenomenon associated with the observed comb structure (see Fig. 4). The emission of discernible pulses can be observed up to a saturation point, corresponding to
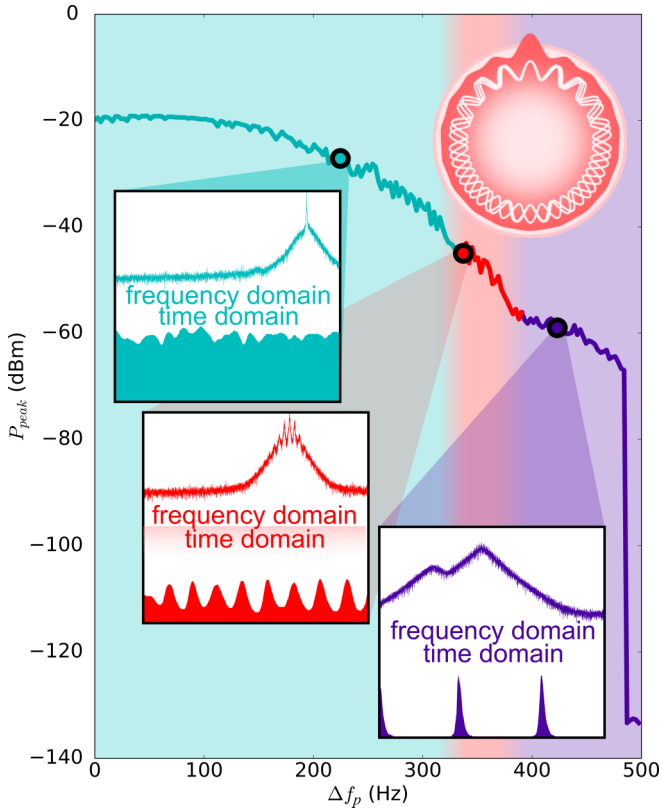

FIG. 5. Maser peak emission (P_{peak}) for various pump frequencies about 31.3377 GHz (Δf_p) for mode A, with $P_{\text{pump}} = 0$ dBm. P_{peak} is defined as the amplitude of the center of the dominant peak in the maser spectrum. Three points are highlighted, one for each regime. The inset panels show maser spectra and associated soliton outputs in the various regimes; (III) single spectral line regime (blue), (II) the dense soliton regime (red), and (I) the sparse soliton regime (purple). Discrete jumps between the regimes can be observed on the spectrum of peak maser output. The top-right inset illustrates the relationship between the comb frequencies, and the intracavity soliton whose existence implies synchronized phases between the comb frequencies.

single-frequency maser emission (cyan in Fig. 3). The relationship between comb shape and soliton emission period is illustrated in Fig. 5, which maps out the three regimes, dependent upon pump frequency or power.

IV. THEORETICAL DESCRIPTION OF THE MASER SOLITON SYSTEM

In a host lattice of sapphire, Fe^{3+} ions effectively act as a three-level system with $|1/2\rangle$ being the ground state, $|5/2\rangle$ the excited state, and $|3/2\rangle$ the intermediate state. A diagram of this ion is shown in Fig. 6. The maser works by pumping ions from the ground state to the excited state from where they then decay into the intermediate state. The stimulated emission between $|3/2\rangle$ and $|1/2\rangle$ leads to masing.

The full description of the system discussed in this work includes a cavity pump mode [whispering gallery modes (WGMs) at 31.337 71 or 31.339 74 GHz], two signal modes (WGMs at 12.038 12 and 12.029 79 GHz), an ensemble of three-level systems, and associated dissipation baths. Generation of solitons in such Λ systems have been considered before in the context of electromagnetically induced transparency (EIT) [24]. In this work, the system is different to EIT as it represents a Λ scheme maser.

A. Simplified system Hamiltonian

For the Fe^{3+} ions in sapphire, the $|5/2\rangle$ state rapidly decays into the $|3/2\rangle$ state and the lifetime of the latter is considerably
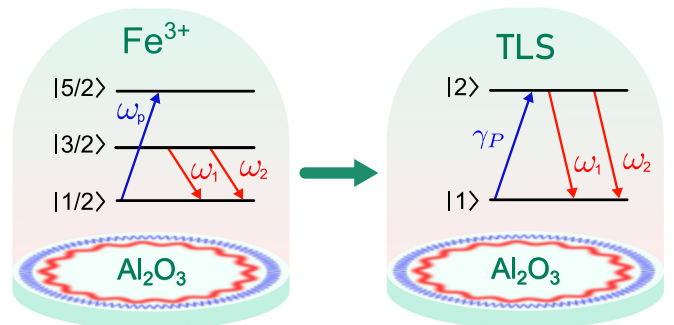

FIG. 6. Schematic of the three-level spin system of the Fe^{3+} ion (left) which leads to masing. The right shows a simplification of the system to a two-level system which is justified by theoretical and experimental observations.

longer. So, observationally, the $N_{|5/2\rangle}$ population is near zero with total population $N \approx N_{|1/2\rangle} + N_{|3/2\rangle}$ at any given time. Furthermore, the dynamics of the pump mode can be adiabatically eliminated as it is dominated by the spin ensemble. Both signal modes are very high Q relative to losses in the Fe^{3+} ensemble, therefore the latter is the dominant source of losses. Additionally, we note that the signal modes are sufficiently far away from each other in frequency space, so that their direct coupling can be neglected. These facts lead to the significantly simplified description of the system as a dual mode laser system with an externally pumped two level system (TLS), with the crystal and the ensemble providing dispersion. The corresponding Hamiltonian (in units $\hbar = 1$) is

$$H = \omega_a \sum_n \sigma_n^+ \sigma_n^- + \sum_{m=1}^{2} \omega_m a_m^\dagger a_m + \sum_{n,m} g_m (\sigma_n^- a_m^\dagger + \sigma_n^+ a_m),$$
(1)

where m is a summation index over the photonic signal modes with resonance frequencies ω_m and creation (annihilation) operators $a_m^\dagger$ (a_m); n is an index over the spin ensemble; σ_n^+, σ_n^-, and σ_n^z are the usual Pauli matrices and g_m are the spin-photon coupling constants. The system is completed by introducing photonic mode loss rates γ_m and TLS emission, decoherence, and pump rates γ_E, γ_D, and γ_P, respectively.

B. Relationship to the Lugiato-Lefever equation

In the limit of a large TLS ensemble, the corresponding Maxwell-Bloch equations (see Chap. 11 in Ref. [25]) could be written as follows,

$$\frac{\partial F_m}{\partial t} + \widetilde{c} \frac{\partial F_m}{\partial z} = (i\omega_m - \gamma_m/2)F_m - ig_m J,$$

$$\frac{\partial J}{\partial t} = (i\omega_a - \gamma_a/2)J + i \sum_{m=1}^{2} g_m F_m D,$$

$$\frac{\partial D}{\partial t} = -\gamma_I (D - D_0) + 2i \sum_{m=1}^{2} g_m (F_m^* J - J^* F_m),$$
(2)

where F, J, and D are proportional to the electric field E_m, the collective atomic polarization, and the population difference, respectively; $\gamma_I = \gamma_P + \gamma_D$; $\gamma_a = \gamma_P + \gamma_D + \gamma_E$; $D_0 = \frac{\gamma_P - \gamma_D}{\gamma_P + \gamma_D}$ is the pump parameter and $\widetilde{c}$ is the effective light velocity, and γ_m is the photonic loss of the mth mode.

The derivation of the Lugiato-Lefever (LLE) equation from the Maxwell-Bloch equations (1) for a case of a single photonic mode is given in Ref. [26] and discussed in other sources, e.g., Ref. [27]. In this work, we show the relationship between the maser soliton system and the LLE as based on the derivation in Ref. [26]. For simplicity we consider only one photonic mode, so that the Maxwell-Bloch equations in the frame associated with angular frequency ω_0 can, by

substituting $J \to iJ$, be written as

$$\frac{\partial F}{\partial t} + \widetilde{c} \frac{\partial F}{\partial z} = -\frac{\gamma}{2} \left[\left(1 + i\frac{2\Omega}{\gamma} \right) F - \frac{2g}{\gamma} J \right],$$

$$\frac{\partial J}{\partial t} = -\frac{\gamma_a}{2} \left[\left(1 + i\frac{2\Omega_a}{\gamma_a} \right) J - \frac{2g}{\gamma_a} F D \right],$$

$$\frac{\partial D}{\partial t} = -\gamma_I \left[D - D_0 + \frac{2g}{\gamma_I} (F^* J + J^* F) \right], \quad (3)$$

where $\Omega = \omega_0 - \omega$ and $\Omega_a = \omega_0 - \omega_a$ are mode and atom detunings. By substituting $D \to D\chi$, $J \to J\xi$, $F \to F\zeta$,

$$\frac{\partial F}{\partial t} + \widetilde{c} \frac{\partial F}{\partial z} = -\frac{\gamma}{2} \left[\left(1 + i\frac{2\Omega}{\gamma} \right) F - \frac{2g\xi}{\gamma\zeta} J \right],$$

$$\frac{\partial J}{\partial t} = -\frac{\gamma_a}{2} \left[\left(1 + i\frac{2\Omega_a}{\gamma_a} \right) J - \frac{2g\chi\zeta}{\gamma_a\xi} F D \right],$$

$$\frac{\partial D}{\partial t} = -\gamma_I \left[D - D_0/\chi + \frac{2g\xi\zeta}{\gamma_I\chi} (F^* J + J^* F) \right]. \quad (4)$$

So, to match the notation in Ref. [26], we have to choose $\frac{2g\xi}{\gamma\zeta} = -2C$, $\frac{2g\chi\zeta}{\gamma_a\xi} = 1$, and $\frac{2g\xi\zeta}{\gamma_I\chi} = \frac{1}{2}$ giving us $\zeta = -\frac{1}{2g}\sqrt{\frac{\gamma_I\gamma_a}{2}}$, $\xi = \frac{C\gamma}{2g^2}\sqrt{\frac{\gamma_I\gamma_a}{2}}$, and $\chi = -\frac{C\gamma\gamma_a}{2g^2}$, giving the following system,

$$\frac{\partial F}{\partial t} + \widetilde{c} \frac{\partial F}{\partial z} = -\frac{\gamma}{2}[(1 + i\theta)F + 2CJ],$$

$$\frac{\partial J}{\partial t} = -\frac{\gamma_a}{2}[(1 + i\Delta)J - FD],$$

$$\frac{\partial D}{\partial t} = -\gamma_I \left[D - D_0/\chi + \frac{1}{2}(F^* J + J^* F) \right], \quad (5)$$

where $\theta = \frac{2\Omega}{\gamma}$ and $\Delta = \frac{2\Omega_a}{\gamma_a}$, which is exactly the starting system for derivation of the LLE in [26]. The only additional parameter is the scaled population inversion parameter D_0/χ which is controlled in our experiment via the high-frequency pump. For the case $D_0 = \chi$ and a circular cavity of radius R, the corresponding LLE is written as

$$\frac{\partial}{\partial \bar{t}} \tilde{F}(\bar{t}, \varphi) = -\tilde{F}(\bar{t}, \varphi) - i\theta_0 \tilde{F}(\bar{t}, \varphi) + i\eta \frac{\beta}{2} \frac{\partial^2}{\partial \varphi^2} \tilde{F}(\bar{t}, \varphi)$$

$$+ i\eta |\tilde{F}(\bar{t}, \varphi)|^2 \tilde{F}(\bar{t}, \varphi), \quad (6)$$

where φ is an angular coordinate, $\eta = -|\Delta|/\Delta$, $\tilde{F} = \sqrt{\frac{2C}{|\Delta|^3}} F$, $\bar{t} = \frac{\gamma}{2} t$, $\theta_0 = \theta - \frac{2C}{\Delta}$, and the dispersion coefficient is

$$\beta = \frac{2C\gamma_a \widetilde{c}^2}{|\Omega_a|^3 R^2}. \quad (7)$$

Although we have demonstrated that the present system is related to the LLE through its connection to the Maxwell-Bloch equations, its dynamics are far more complicated. This additional dynamics makes the system deviate from expected behavior of typical LLE systems.

C. Distinguishing features of the maser soliton system

While in optics, a system may be represented by a pure one-dimensional (1D) circular cavity, our sapphire resonator is a large 3D cavity with a more complicated wave structure involving some dynamics of two additional degrees of freedom. Its large spatial footprint leads to significant spin ensemble broadening. A more complicated level structure of

the Fe^{3+} ensemble induces additional decoherence effects through interactions with higher-energy levels. The same is true for the high-frequency pump mode exhibiting additional dynamics potentially involving decoherence effects; in optical counterparts involving only the Kerr nonlinearity this additional decoherence is avoided all together. Furthermore, apart from the target Fe^{3+} ensemble, the crystal hosts additional spin ensembles (e.g., chromium) involving a spin-spin interaction as well as interactions with nuclei spin which is the main source of local decoherence in our target spin system. Clearly, the system is highly susceptibility to external magnetic fluctuations due to the fact that it is based on a spin ensemble. Finally, there are two cavity modes involved which are both coupled to the same spin ensemble and thus can interact. Overall, all these additional effects give observed deviations from the picture expected from the LLE equation.

V. CONCLUSION

These observations provide a window into the spontaneous self-organization behaviors within this nonlinear many-body spin system, worthy of further study. The system may be related to the Lugiato-Lefever equation (a damped, driven, nonlinear wave equation) for which temporal solitons on top of a continuous-wave pump are a solution and which likewise describes the dynamics of Kerr frequency combs [27]. Due to various inhomogeneities of the spin ensemble, and imperfections in the crystal itself, inhomogeneity and nonperiodicity can be observed in the soliton trains. These temporal results are more thoroughly presented in the Appendixes. The production of this maser-based comb structure, and associated soliton pulse train, in a simple sapphire system has great potential for further investigation, both theoretically, into the behavior of the dissipative masing system, and into the potential applications of this comb, for example in precision spectroscopy [6], tunable narrowband microwave signal generation [28], or reconfigurable rf filtering [29]. A detailed characterization of the soliton evolution and comb structure will be undertaken in the future.

APPENDIX A: RESULTS AT 4 K

Figure 7 presents the power dependence of masing, for modes A and B. Unlike the masing results at mK, shown in the main text, there is no two-peak structure present, and although there are modulation sidebands, a fine frequency comb is not produced as in the mK case. Figure 8 presents the response of masing on modes A and B when the pump frequency is swept. As in the mK case, the doublet structure of the pump mode is evident.

APPENDIX B: FURTHER RESULTS AT mK

Figures 9 and 10 present masing observed at mK, that is, between 16 and 50 mK after transient heating, over a range of pump frequencies and at different incident powers. Figure 9 presents results when pump mode 1 was pumped and Fig. 10 presents results when pump mode 2 was pumped. Figures 11 and 12 display the time-series soliton output.
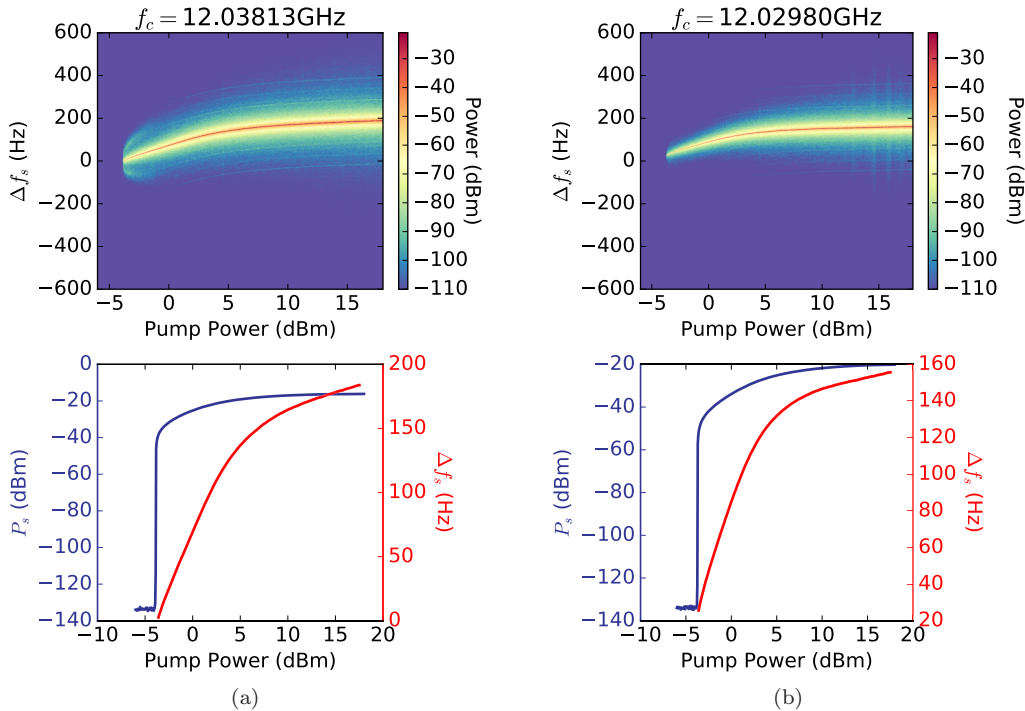

FIG. 7. Pumping on the first pump mode at an array of pump powers for modes A (a) and B (b). Measurements taken at 4 K. Power at the signal output is gauged by the color bar and the masing peak can be tracked relative to the center of the measurement spectrum (Δf_s). The bottom plots isolate the frequency shift (Δf_s, red) and maximum power (P_s, purple) of the maser peaks, depending on incident pump power.
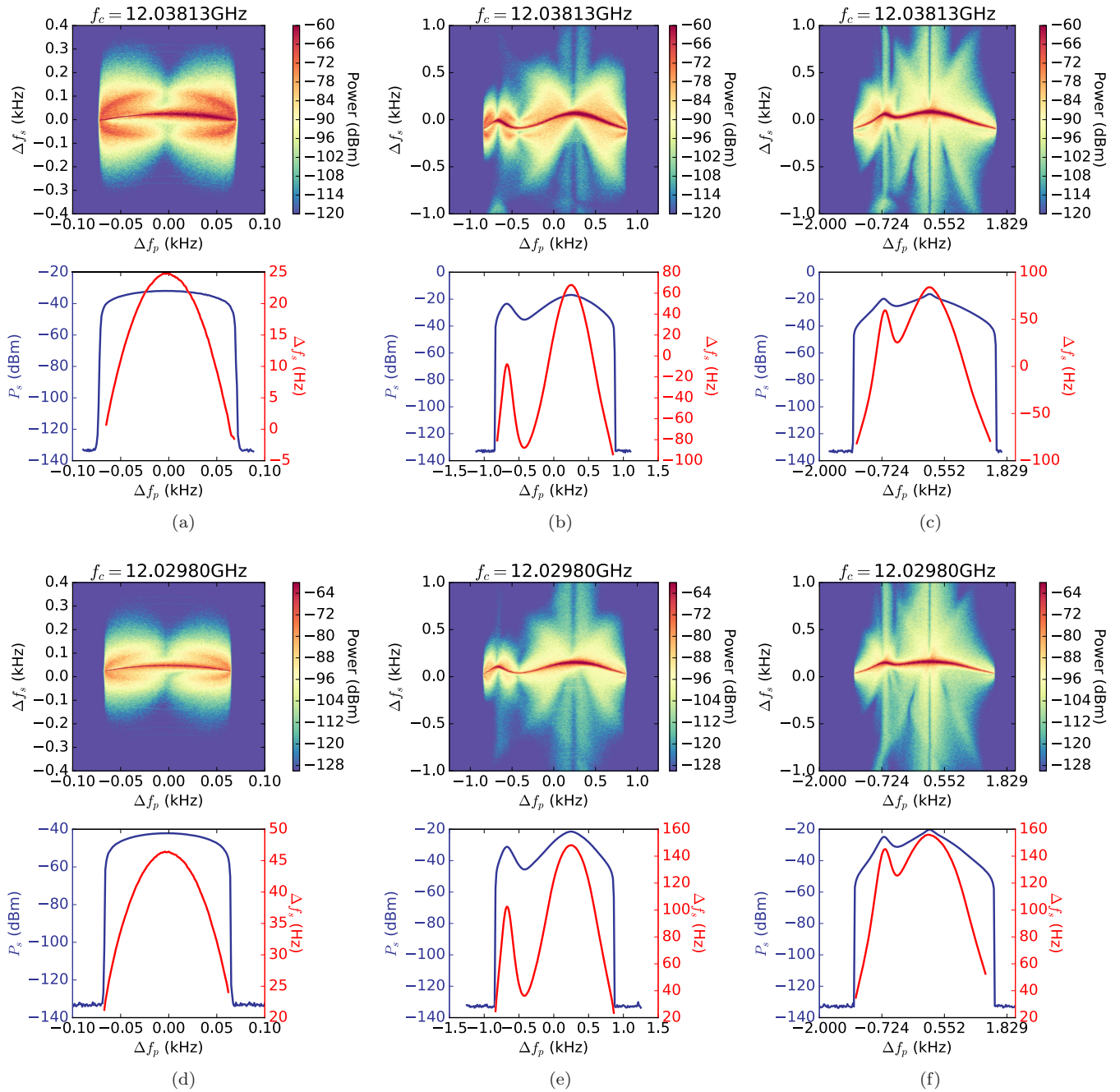
FIG. 8. Pumping on the first pump mode at an array of pump frequencies about f_p for modes A [(a)–(c)] and B [(d)–(f)] with pump power set to -33, -20, and -13 dBm, respectively. Measurements taken at 4 K. Power at the signal output is gauged by the color bar and the masing peak can be tracked relative to the center of the measurement spectrum (Δf_s). The bottom plots isolate the frequency shift (Δf_s, red) and maximum power (P_s, purple) of the maser peaks, depending on incident pump frequency.
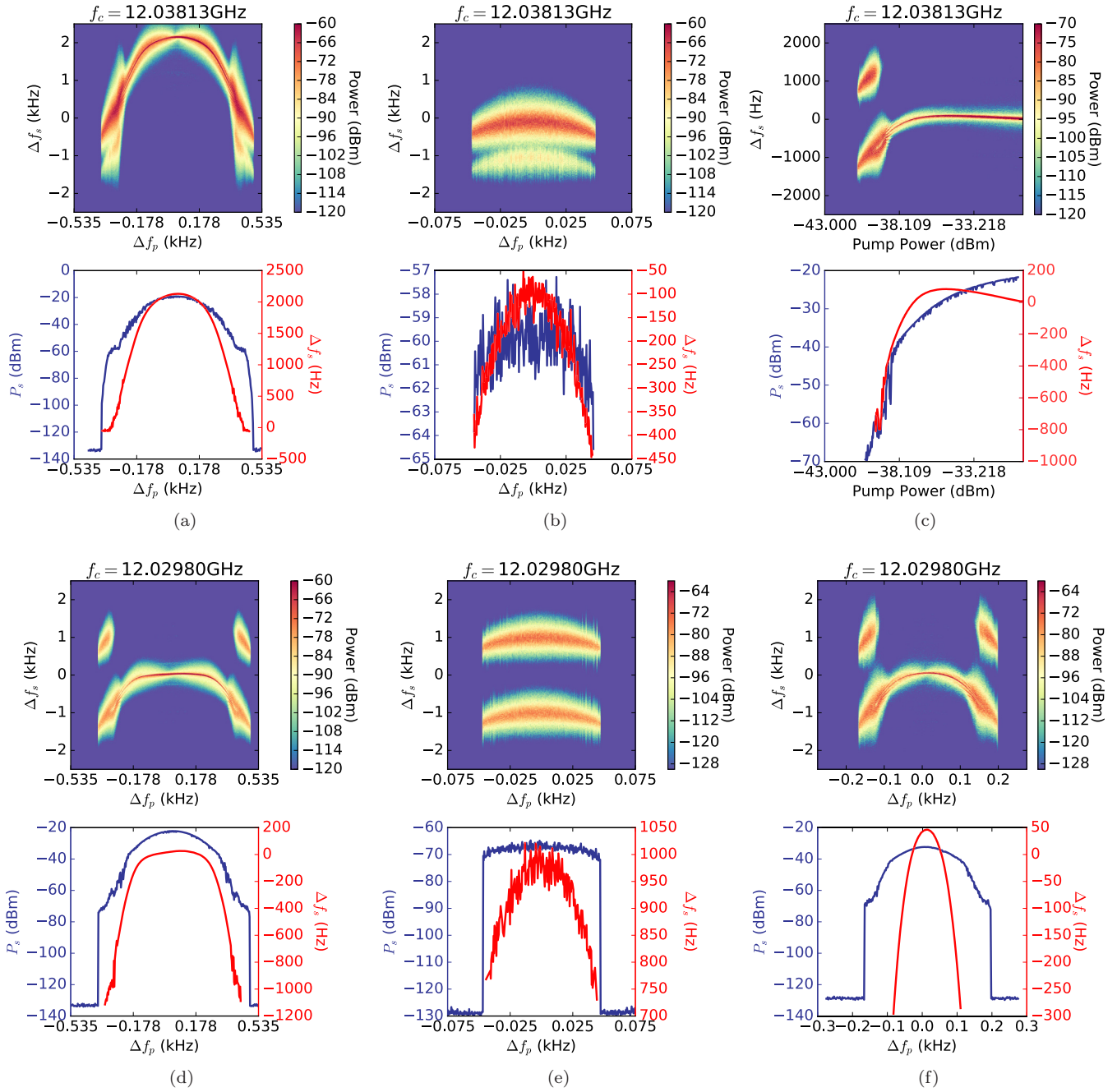
FIG. 9. Pumping on the first pump mode at an array of pump frequencies about f_p for modes A [(a), (b)] and B [(d)–(f)] with pump power set to -31, -41, and -37 dBm (mode B only), respectively. Measurements taken at mK. Power at the signal output is gauged by the color bar and the masing peak can be tracked relative to the center of the measurement spectrum (Δf_s). The bottom plots isolate the frequency shift (Δf_s, red) and maximum power (P_s, purple) of the maser peaks, depending on input pump frequency. The dependence of mode B upon pump power is represented in (c), but neglected for mode A, as this is shown in the main text.
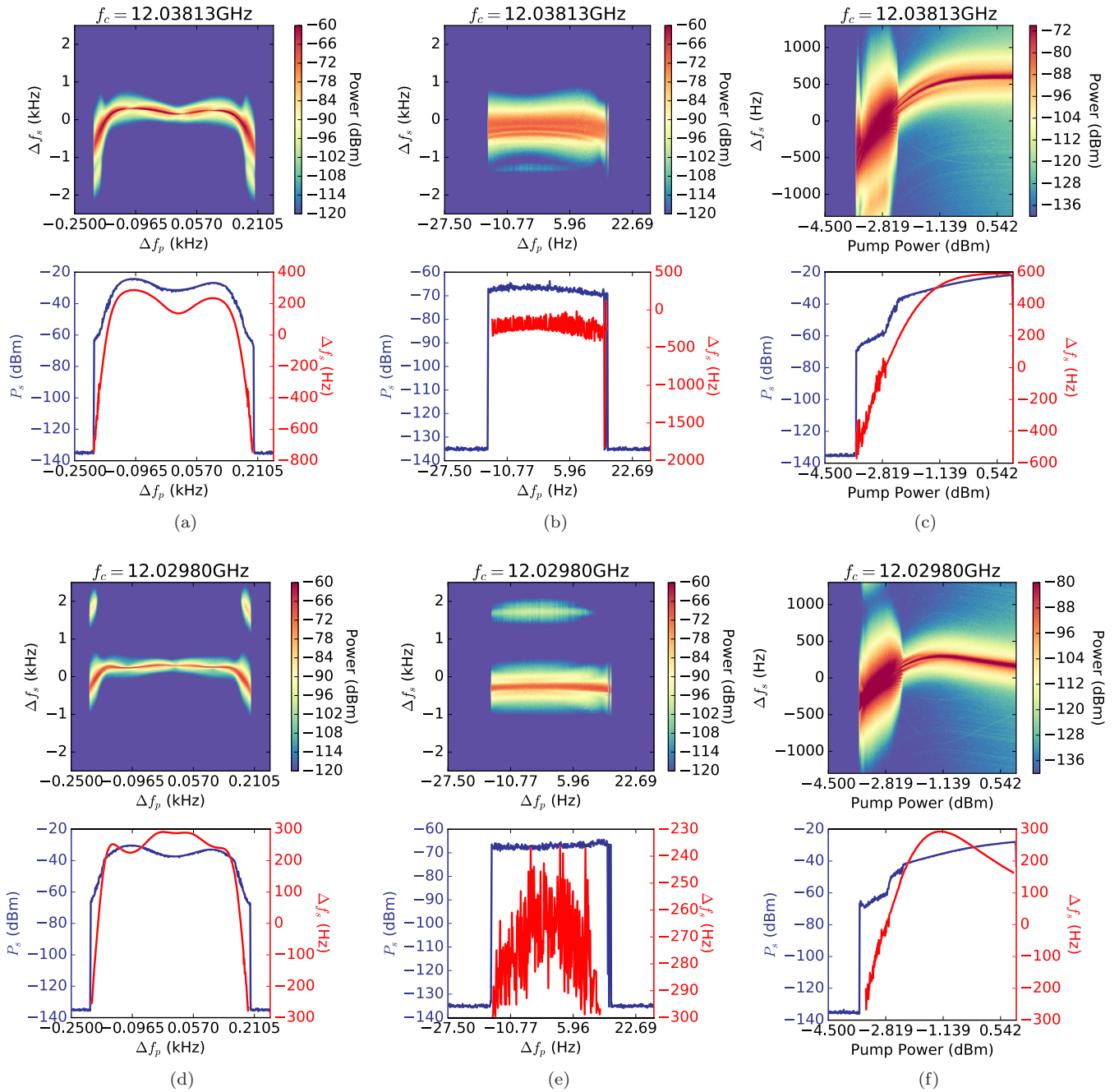
FIG. 10. Pumping on the second pump mode at an array of pump frequencies about f_p for modes A [(a), (b)] and B [(d), (e)] with pump power set to -31 and -34.5 dBm, respectively. Measurements taken at mK. Power at the signal output is gauged by the color bar and the masing peak can be tracked relative to the center of the measurement spectrum (Δf_s). The bottom plots isolate the frequency shift (Δf_s, red) and maximum power (P_s, purple) of the maser peaks, depending on input pump frequency. The dependence of modes A and B upon pump power is also represented [(c) and (f)].
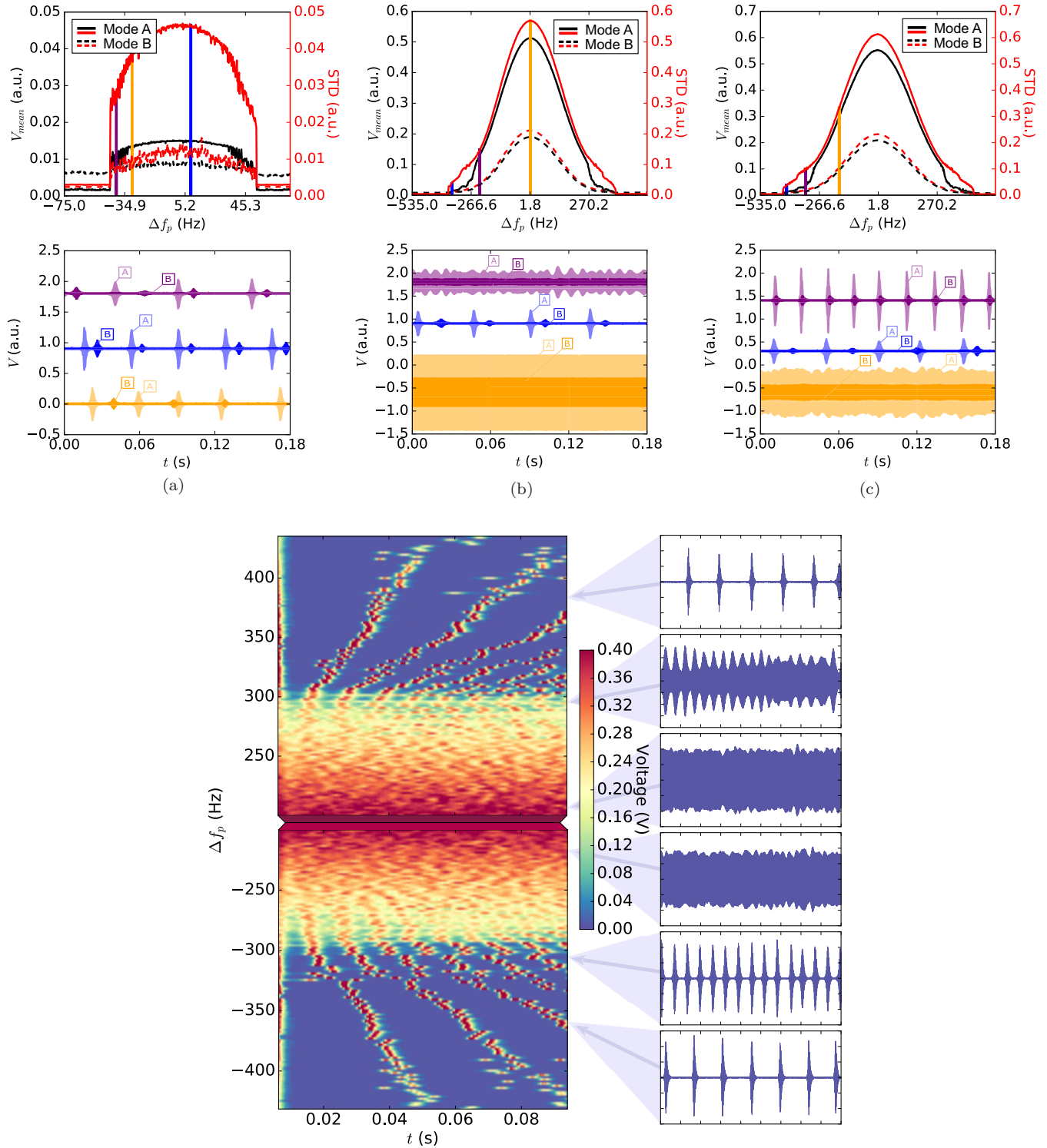
FIG. 11. At incident powers of −41, −36, and −31 dBm [(a)–(c)], the pump frequency was swept around pump mode 1 (Δf_p), and solitons were observed at the mixed down mode outputs A and B. The top plots record the standard deviation (red) and mean output voltage (black) of the soliton train (or continuous wave) emanating from the crystal at the signal modes. Depending on the input pump frequency, solitons may be emitted discretely in pulses, or the output may evolve into a continuous wave. The bottom plot (right) presents snapshots of the soliton output produced at −31 dBm incident power [corresponding to (c), output A], for various Δf_p. In the color density plot (left), traces are aligned to the first pulse to illustrate intersoliton-period dependence upon pump frequency.
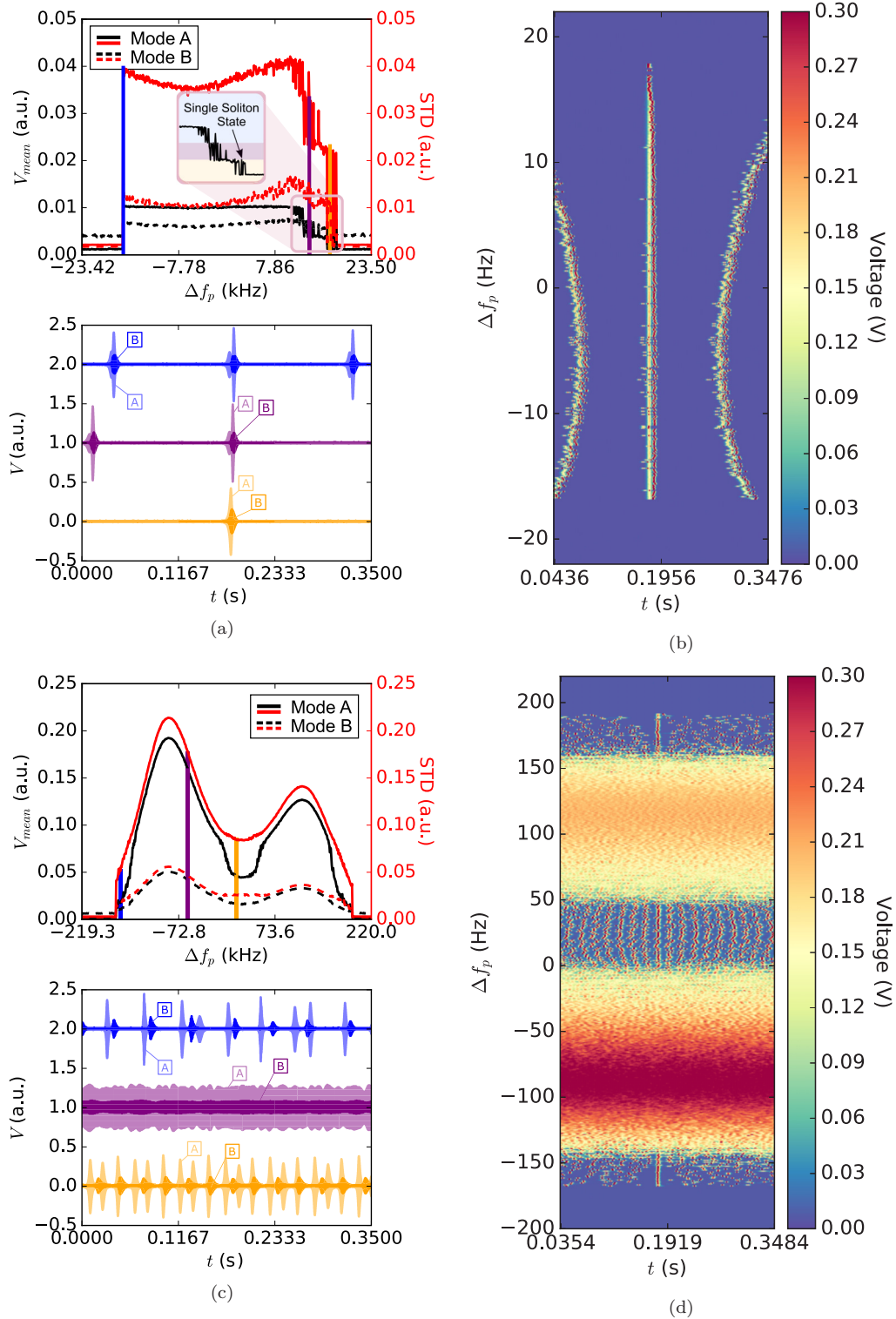
(a)

(b)

(c)

(d)

FIG. 12. At incident powers of -34.5 dBm [(a) and (b)] and -32 dBm [(c) and (d)], the pump frequency was swept around pump mode 2, and solitons were observed at the mixed down mode outputs A and B. The left plots record the standard deviation (red) and mean output voltage (black) of the soliton train (or continuous wave) emanating from the crystal at the signal modes. (b) and (d) present snapshots of the soliton outputs produced at -34.5 and -32 dBm incident power, from mode A and B, respectively, for various Δf_p. In the latter, we can observe the pump twice breaching the power level at which discrete soliton emission can be sustained, caused by the doublet shape of the pump mode. Highlighted in (a), the mean output voltage shows clear jumps at certain Δf_p steps, which suggests the elimination of one intracavity soliton at each step. The yellow region (corresponding to the yellow time trace) is therefore representative of the single soliton state.

[1] Th. Udem, R. Holzwarth, and T. W. Hänsch, Optical frequency metrology, Nature (London) **416**, 233 (2002).

[2] S. A. Diddams, K. Vahala, and Th. Udem, Optical frequency combs: Coherently uniting the electromagnetic spectrum, Science **369**, eaay3676 (2020).

[3] M. Kourogi, K. Nakagawa, and M. Ohtsu, Wide-span optical frequency comb generator for accurate optical frequency difference measurement, IEEE J. Quantum Electron. **29**, 2693 (1993).

[4] Th. Udem, J. Reichert, R. Holzwarth, and T. W. Hänsch, Accurate measurement of large optical frequency differences with a mode-locked laser, Opt. Lett. **24**, 881 (1999).

[5] J. Reichert, R. Holzwarth, Th. Udem, and T. W. Hänsch, Measuring the frequency of light with mode-locked lasers, Opt. Commun. **172**, 59 (1999).

[6] S. A. Diddams, L. Hollberg, and V. Mbele, Molecular fingerprinting with the resolved modes of a femtosecond laser frequency comb, Nature (London) **445**, 627 (2007).

[7] S. Witte, Deep-ultraviolet quantum interference metrology with ultrashort laser pulses, Science **307**, 400 (2005).

[8] X. Yi, Q.-F. Yang, K. Y. Yang, M.-G. Suh, and K. Vahala, Soliton frequency comb at microwave rates in a high-Q silica microresonator, Optica **2**, 1078 (2015).

[9] A. Barthelemy, S. Maneuf, and C. Froehly, Propagation soliton et auto-confinement de faisceaux laser par non linearité optique de Kerr, Opt. Commun. **55**, 201 (1985).

[10] C. Cambournac, H. Maillotte, E. Lantz, J. M. Dudley, and M. Chauvet, Spatiotemporal behavior of periodic arrays of spatial solitons in a planar waveguide with relaxing Kerr nonlinearity, J. Opt. Soc. Am. B **19**, 574 (2002).

[11] F. Leo, S. Coen, P. Kockaert, S.-P. Gorza, P. Emplit, and M. Haelterman, Temporal cavity solitons in one-dimensional Kerr media as bits in an all-optical buffer, Nat. Photon. **4**, 471 (2010).

[12] T. Herr, V. Brasch, J. D. Jost, C. Y. Wang, N. M. Kondratiev, M. L. Gorodetsky, and T. J. Kippenberg, Temporal solitons in optical microresonators, Nat. Photon. **8**, 145 (2013).

[13] T. Fortier and E. Baumann, 20 years of developments in optical frequency comb technology and applications, Commun. Phys. **2**, 153 (2019).

[14] P.-Y. Bourgeois, N. Bazin, Y. Kersalé, V. Giordano, M. E. Tobar, and M. Oxborrow, Maser oscillation in a whispering-gallery-mode microwave resonator, Appl. Phys. Lett. **87**, 224104 (2005).

[15] D. L. Creedon, K. Benmessaï, W. P. Bowen, and M. E. Tobar, Four-Wave Mixing from Fe^{3+} Spins in Sapphire, Phys. Rev. Lett. **108**, 093902 (2012).

[16] D. L. Creedon, K. Benmessai, and M. E. Tobar, Frequency Conversion in a High Q-Factor Sapphire Whispering Gallery Mode Resonator due to Paramagnetic Nonlinearity, Phys. Rev. Lett. **109**, 143902 (2012).

[17] K. Benmessai, M. E. Tobar, N. Bazin, P.-Y. Bourgeois, Y. Kersalé, and V. Giordano, Creating traveling waves from standing waves from the gyrotropic paramagnetic properties of Fe^{3+} ions in a high-Q whispering gallery mode sapphire resonator, Phys. Rev. B **79**, 174432 (2009).

[18] M. Goryachev, W. G. Farr, D. L. Creedon, and M. E. Tobar, Spin-photon interaction in a cavity with time-reversal symmetry breaking, Phys. Rev. B **89**, 224407 (2014).

[19] D. L. Creedon, Y. Reshitnyk, W. Farr, J. M. Martinis, T. L. Duty, and M. E. Tobar, High Q-factor sapphire whispering gallery mode microwave resonator at single photon energies and millikelvin temperatures, Appl. Phys. Lett. **98**, 222903 (2011).

[20] W. G. Farr, D. L. Creedon, M. Goryachev, K. Benmessai, and M. E. Tobar, Ultrasensitive microwave spectroscopy of paramagnetic impurities in sapphire crystals at millikelvin temperatures, Phys. Rev. B **88**, 224426 (2013).

[21] D. L. Creedon, K. Benmessai, M. E. Tobar, J. G. Hartnett, P.-Y. Bourgeois, Y. Kersale, J.-M. Le Floch, and V. Giordano, High-power solid-state sapphire whispering gallery mode maser, IEEE Trans. Ultrason., Ferroelectr. Freq. Control **57**, 641 (2010).

[22] L. S. Kornienko and A. M. Prokhorov, Electronic paramagnetic resonance of the Fe^{3+} ion in corrundum, J. Exp. Theor. Phys. **40**, 1594 (1961) [Sov. Phys. JETP **13**, 1120 (1961)].

[23] K. Benmessai, D. L. Creedon, M. E. Tobar, P.-Y. Bourgeois, Y. Kersalé, and V. Giordano, Measurement of the Fundamental Thermal Noise Limit in a Cryogenic Sapphire Frequency Standard Using Bimodal Maser Oscillations, Phys. Rev. Lett. **100**, 233901 (2008).

[24] Y. Wu and L. Deng, Ultraslow bright and dark optical solitons in a cold three-state medium, Opt. Lett. **29**, 2064 (2004).

[25] L. Lugiato, F. Prati, and M. Brambilla, *Nonlinear Optical Systems* (Cambridge University Press, Cambridge, UK, 2015).

[26] F. Castelli, M. Brambilla, A. Gatti, F. Prati, and L. A. Lugiato, The LLE, pattern formation and a novel coherent source, Eur. Phys. J. D **71**, 84 (2017).

[27] L. A. Lugiato, F. Prati, M. L. Gorodetsky, and T. J. Kippenberg, From the Lugiato–Lefever equation to microresonator-based soliton Kerr frequency combs, Philos. Trans. R. Soc. A **376**, 20180113 (2018).

[28] N. R. Newbury, Searching for applications with a fine-tooth comb, Nat. Photon. **5**, 186 (2011).

[29] A. A. Savchenkov, A. B. Matsko, V. S. Ilchenko, I. Solomatine, D. Seidel, and L. Maleki, Tunable Optical Frequency Comb with a Crystalline Whispering Gallery Mode Resonator, Phys. Rev. Lett. **101**, 093902 (2008).